Global Journal of Engineering Science and Research Management

THE SEVEN CASES UNSTRUCTURED TRIANGULATION TECHNIQUE FOR RADIATIVE HEAT TRANSFER APPROXIMATION IN AN ETHYLENE FURNACE CRACKER

Zuraida Abal Abas*, Zaheera Zainal_Abidin, Abdul Samad Shibghatullah, Ahmad Fadzli Nizam Abd Rahman, Hidayah Rahmalan, Nur Farraliza Mansor.
*Department of Intelligent Computing and Analytics, Faculty of Information and Communication Technology,
Universiti Teknikal Malaysia Melaka, 76100 Durian Tunggal, Melaka, Malaysia.
zuraidaa@utem.edu.my

ABSTRACT

Radiative heat distribution inside an ethylene cracker furnace is often modelled using the finite volume and finite element methods. In both cases, meshes in the form of rectangles and triangles are needed to serve as the approximating points in the domain. In this paper, a new method called the Seven Cases Unstructured Triangulation Technique (7CUTT) is proposed for meshing the domain inside the cracker furnace, integrated with the deployment of sensors on the wall to obtain the boundary value. 7CUTT is an enhanced version of the Standard Advancing Front Technique (SAFT) which two normal cases in SAFT are extended to the total of seven cases for consideration during the element creation procedure for initial mesh generation. The focus of this method is to construct the initial triangular meshes with the requirement of (1) having the location of sensors deployed along the wall as boundary nodes as well as forming boundary elements, (2) generating nodes at a certain boundary with linearly different lengths of boundary edges as interior gradation controls and (3) constructing the triangular element directly in every iteration without having to re-order the Front or delete the existing elements. There are three contributions from this paper, the first one is the introduction of seven extended cases for consideration for the element creation procedure, the second is the layer concept to generate edges with linearly different lengths and the third is the post-processing mesh procedure to improve the quality of the mesh that is suitable for 7CUTT. The final mesh is obtained once the post-processing procedure of improving the mesh quality is applied to the initial mesh. 7CUTT provides the framework for the heat to be approximated using the discrete ordinate method, which is a variant of the finite volume method. Simulation results produced using FLUENT support the findings for effectively approximating the

flue gas temperature distribution, the circumferential radiative heat flux incident at the reactor coils as well as the circumferential reactor coil temperature in the furnace at the end of the study.

INTRODUCTION

Ethylene is an important chemical compound produced in the petrochemical industry which is produced from the steam cracking process in ethylene cracker furnaces [1]. In steam cracking, heat is used for breaking or cracking down the saturated hydrocarbon or feedstocks into smaller hydrocarbon in the coils or reactor tubes, which eventually produces desired products such as ethylene.

Radiation is a heat transfer mode which plays a significant role in ethylene production. It has been noted in [2] that 90% of the heat transfers in the furnace involve radiation. Radiation is caused by energy emission in the form of electromagnetic waves or streams of photons [3]. The burners which are located on the floor near the furnace wall heat up the furnace. This happens because the combustion process carried out in the burner results in flames and the release of its hot flue gas. The radiative heat from the furnace wall and hot flue gas is transferred to reactor tubes/coils.

A structured or unstructured triangular mesh formation is an important step for approximating solutions to boundary value problems[4-10]. One such method is the advancing front technique, whose key algorithmic step is the appropriate introduction of new elements to the empty region [11]. The method places a new element by considering ideal points to be generated as well as the existing nodes in the circle to be constructed. The centre of the circle is the ideal point and the radius is calculated based on the empirical rules for the element creation procedure. The advancing front technique is guaranteed to preserve boundary integrity as well as having the capacity to create triangular elements with high aspect ratios in the boundary-layer region [12]. It must be noted that triangle or triangular element is one of the geometry features that is widely used in many studies such as radiative heat transfer, fingerprint, face, digit recognition and vehicle detection [13-20].

In [21], the triangulation process of a closed two dimensional region was proposed. The method involves steps for generating the elements and reading their boundary values, smoothing the grids and labelling the nodes. The method focuses on node renumbering to make way for the Cuthill-McKee algorithm [21] in estimating the matrix bandwidth [22], to be applied for producing smaller bandwidths in order to reduce storage and computation time.

Sazanov and Wang et al. [23] proposed a model which generates near boundary elements with their own modified form of advancing front techniques to allow a new node to be located based on the length of the adjacent edges in its front and the angle between the edges. The points for insertion in this model are determined based on a repeated

procedure according to the angle between the edges and the range of a number of nodes. The model also stitches together two different meshes to provide a consistent mesh for the whole domain.

Ito et al. [24] proposed a robust and low computational approach for a parallel framework to generate large-scale meshes for partitioning a coarse tetrahedral mesh into a number of sub-domains using a partitioning algorithm called METIS. The model is based on the parallel advancing front method to generate the volume mesh in each sub-domain.

In [25], the author highlighted three cases as being possible during the element creation procedure:
  (1) A new element is created with a new node as a vertex in which the new node is joined to the edge being considered.
  (2) An already existing Front node satisfying certain conditions in the proximity of the edge being considered is used to create a new element.
  (3) Neither of the cases above in which an efficient algorithm of mesh generation should be able to tackle such a problem.

In the present paper, a new algorithm called the Seven Cases Unstructured Triangulation Technique (7CUTT) is introduced, for producing initial unstructured grids based on seven categories of cases. These seven categories of cases are extensions of the normal cases as in [12, 25] and are able to solve the problems highlighted in [25], specifically the third point above. The technique takes into account the deployment of sensor nodes as boundary nodes which supply input values into the system. The technique makes use of the layer concept. Radiative heat transfer in the ethylene cracker furnace can be modelled using the Discrete Ordinate Method by transforming the radiative heat equations into a set of simultaneous partial differential equations based on a discrete representation of the directional variation of the radiative intensity [3].

PROBLEM STATEMENT
Problem formulation and problem statement can be regarded as significant part in any research study [26-34]. In this research, the problem can be stated as follows: Given a set of sensors distributed along the wall of the ethylene furnace, in what way can the sensors be deployed to provide input in the form of boundary values to approximate the temperature of the flue gas inside the furnace, the radiative heat flux incident at the reactor coils and the temperature of the skin of the reactor coil?
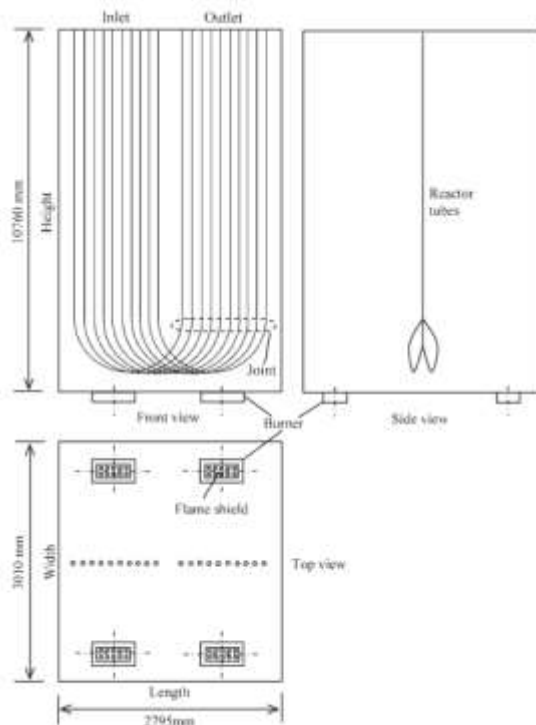
Global **J**ournal of **E**ngineering **S**cience and **R**esearch **M**anagement

Figure 1a. The illustration of an ethylene furnace taken from [35]

Global Journal of Engineering Science and Research Management
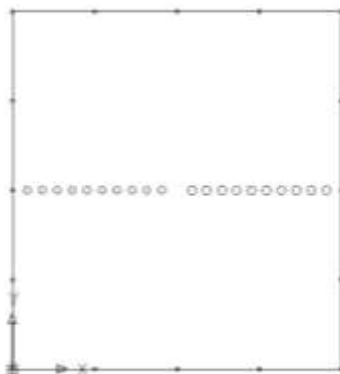

Figure 1b. The top view of the furnace with sensors placed along the wall taken from [35]

In this problem, the approximation based on the two-dimensional cross-section of the furnace involving cases with an arbitrary number of coils is discussed. Figure 1a shows the illustration of an ethylene furnace with a set of ten coils taken from [35]. Each complete coil has an inlet and an outlet. Therefore, from the top view of the furnace considering it is a two-dimensional problem, it can be seen that there are 20 circles in the centre of the domain. The ten circles on the left side of the furnace represent the inlet reactor coils while the ten circles on the right side of the furnace represent the outlet reactor coils.

Approximation to the boundary value problem involves three processes, namely, structured or unstructured grid generation, physical process model development and discretization using finite difference, finite volume or finite elements. In some specific problems, the process of generating the grid is identified to be affected if sensors are deployed. The values provided by the sensors are crucial, as they form the boundaries in the domain. Therefore, their locations in the domain determine the overall shape of the triangular mesh which, in turn, affects the temperature approximations.

The focus of the present paper is to improve the initial unstructured grids by modifying the existing standard method in order to arrive at a mesh which satisfies the requirement of having the sensors placed at the boundary as the nodes for the boundary elements. As a conceptual model study, the set of 16 sensors are assumed to be placed on the wall as illustrated in Figure 1b. At the same time, the method needs to be able to have interior gradation control as well as being able to solve the current element creation problem described in section 1 above.

Global **J**ournal of **E**ngineering **S**cience and **R**esearch **M**anagement

STANDARD ADVANCING FRONT TECHNIQUE AND NUMERICAL METHOD

The general basic step of the standard Advancing Front Technique (SAFT)

The advancing front technique is one kind of unstructured triangulation grid generation method which preserves boundary integrity as well as having the capacity to create the clustering high aspect-ratio triangles in boundary-layer regions [12]. The boundary curves are discretized by dividing them into straight line segments or edges where nodes are placed on each of the segments or edges. An edge is denoted as (a,b) which means that the edge is formed by nodes a and b. Figure 2a illustrates a simple two dimensional domain with connected boundary curves while Figure 2b illustrates the discretized boundary curves into a set of edges denoted by $(1,2)$, $(2,3)$, $(3,4)$, until $(10,1)$.
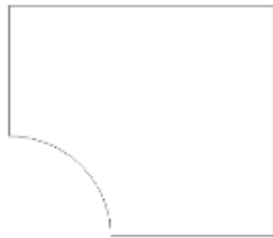

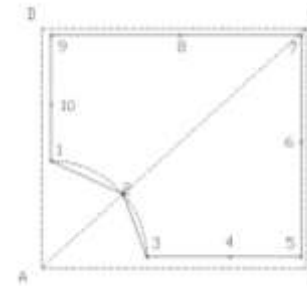Figure 2a. A two dimensional domain with connected boundary curves

Figure 2b. A set of edges forming initial Front and the background grid consisting of triangles ABC and ADC

Front [12, 25] is a list or a set of active edges which is currently available for element triangulation. Referring to Figure 2b, all the edges which are $(1,2)$, $(2,3)$, $(3,4)$, until $(10,1)$ form the first or initial Front. The Front is updated continuously when a triangular element is created. This can be seen in Figure 3, taken from [36]. It must be noted that all the edges belonging to the current Front are considered as active edges while edges that are deleted from the current Front list are considered as passive edges. Any nodes which compose the active edges in the current position of the Front list are also known as active nodes.
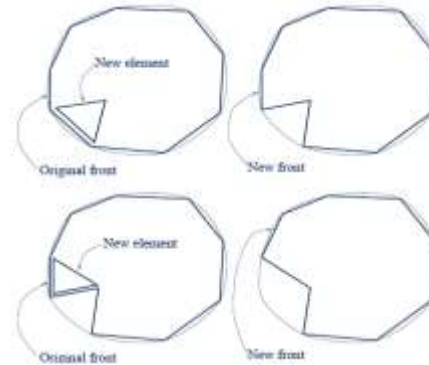
Figure 3. The illustration of elements with regards to Front, taken from [36]

The main approach to controlling the grid in terms of the size and shape of the triangular element involves the definition of the required grid-cell characteristic through background grid generation [11, 12, 25, 37-40]. The grid-cell characteristics, known as grid cell parameters, are the size parameter δ, the stretching s and finally the orientation of the cells ϕ [12]. For example, Figure 2b illustrates the background grid consisting of two triangles ABC and ADC. The grid cell parameters are required to be specified at each node forming the background grid where in this example at nodes A, B, C and D. In the creation of the triangular element, once the edge is selected from the Front for triangulation, the position of 'ideal' point (IP)[12] on the perpendicular bisector of the edge is computed in such a way that an equilateral triangle is formed with IP as the third vertex. Figure 4a illustrates a selected edge, which is (a,b) and the position of the IP.
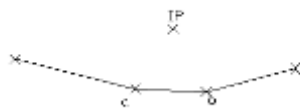

Figure 4a. The selected edge (a,b) and the position of IP

Figure 4b. A circle is constructed with its centre at IP and the radius of the circle following the empirical rule.

Grid cell parameters for all nodes in the Front are interpolated [12]. The edge with the shortest length l in the

Global Journal of Engineering Science and Research Management

Front is selected as a departure zone in order to create the triangular element. In order to obtain δ for the next step of calculation, the interpolated values of δ corresponding to the two nodes of the edge are averaging. A circle with centre at IP is constructed with the following empirical formula for the radius, $r = 0.8 * \delta'$, where [12]

$$\delta' = \begin{cases} 0.55*l; & \delta < 0.55*l \\ \delta; & 0.55*l \leq \delta \leq 2.0*l \\ 2.0*l; & \delta > 2.0*l \end{cases} \tag{1}$$

Figure 4b illustrates a circle with its centre at IP and the radius of the circle following the empirical rule. Active nodes that lie within the circle are searched (if any) and their distances from IP are listed. The best candidate for the third vertex of the triangular element would be the closest one to the IP. The equilateral triangle is constructed if there are no such active nodes lying within the circle. However, the validity of the IP becoming the node must be checked, by which it needs to satisfy the following conditions [12]:

(1) The coordinate of IP does not lie inside another existing triangular element,
(2) There is no intersection between the side of the new triangular element and any existing sides of the active front.
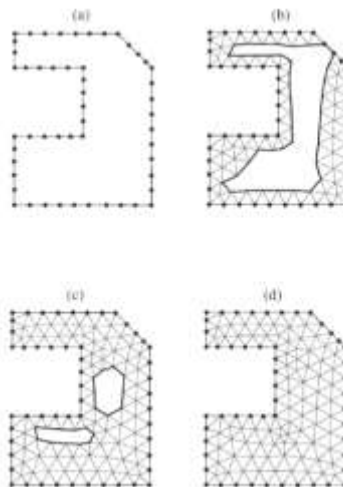

Figure 5. The illustration of the Front 'marching' process into the interior of the domain, taken from [41]

Generally, the Front progresses into the interior of the domain in a 'marching' [12, 41] process as a result of

Global Journal of Engineering Science and Research Management

producing a triangular element in which new nodes and edges are created and at the same time old related edges are deleted, as illustrated in Figure 5. The new triangular element is constructed by two nodes of a segment of a Front and another node, either a newly created one or one that has already existed in the Front. This process is continued until there are no longer any active edges in the Front list.

The concept of radiation

Radiation is emitted at a high rate by materials at a high temperature. Emissive power E (W/m^2) is the rate of heat flow per unit surface area emitted by a radiating surface. For a black body, emissive power, E_b is given by [42]

$$E_b = \sigma T^4 \tag{2}$$

In equation (2), $\sigma = 5.67 x 10^{-8}$ (W/m^{2}K^4) is Stefan-Boltzmann's constant and T (K) is absolute temperature. The intensity I (W/m^2.sr) is the rate of heat flow received per unit area perpendicular to the rays and per unit solid angle. The formula for intensity of the black body, I_b is [42]

$$I_b = E_b / \pi = \sigma T^4 / \pi \tag{3}$$

Equation (3) is used to compute the emitted intensity from surfaces and fluids. However, for a real surface or gray surface, the emissive power, E_s with surface emissivity ε is given by [42]

$$E_s = \varepsilon \sigma T^4 \tag{4}$$

Its emitted intensity I_s is the product of its surface emissivity and the black body intensity [42]

$$I_s = \varepsilon I_b = \varepsilon \sigma T_s^4 / \pi \tag{5}$$

When combustion occurs, there exist large amounts of carbon dioxide and water vapour where these combustion products are both strong absorbers/emitters in the infrared part of the spectrum and this fluid is termed as a participating medium [42, 43]. The interaction between participating fluid medium and radiation can be measured in terms of the absorption coefficient, κ (m^{-1}) and its scattering coefficient, σ_s (m^{-1}) where the sum of these two properties is called the extinction coefficient $\beta = \kappa + \sigma_s$ [42].

The general relationship that governs the changes in radiation intensity at a point along a radiation ray due to emission, absorption and scattering in a fluid medium is as follows [3, 42, 44]

$$(\mathbf{\Omega}.\nabla) I(\mathbf{r},\mathbf{\Omega}) = -(\kappa + \sigma_s) I(\mathbf{r},\mathbf{\Omega}) + \kappa I_b(\mathbf{r}) + \frac{\sigma_s}{4\pi} \int_{\Omega'=4\pi} I(\mathbf{r},\mathbf{\Omega}) \Phi(\mathbf{\Omega'} \to \mathbf{\Omega}) d\mathbf{\Omega'} \tag{6}$$

In the above equation, $I(\mathbf{r},\mathbf{\Omega})$ is the intensity of radiation at a location indicated by position vector $\mathbf{r}$ in direction

Global Journal of Engineering Science and Research Management

Ω while $\Phi\left(\Omega'\rightarrow\Omega\right)$ is scattering phase function from the incoming direction, Ω' to the outgoing direction, Ω [3, 42, 44]. The term at the left side of equation (6) represents the gradient of intensity following the direction Ω while the first, second and third terms at the right-hand side equation are the changes in radiation intensity due to absorption and out-scattering, emission and in-scattering respectively. Equation (6) is integrated over each triangular element in the mesh and it is subject to the boundary conditions as follows [3, 42, 44]

$$I\left(\mathbf{r_w},\Omega^+\right)=\varepsilon I_b\left(\mathbf{r_w}\right)+\frac{(1-\varepsilon)}{\pi}\int_{\mathbf{n}.\Omega^-<0}I\left(\mathbf{r_w},\Omega^-\right)|\mathbf{n}\cdot\Omega^-/\mathrm{d}\Omega^- \tag{7}$$

In equation (7), $\mathbf{r_w}$ is a position vector for a point on a diffusively emitting and reflecting gray surface, $\mathbf{n}$ is outward surface normal while Ω^+ and Ω^- is leaving and arriving radiation intensity directions respectively.

The spatial derivative in equation (6) can be written as the following in the Cartesian coordinate [44]

$$\left(\Omega.\nabla\right)I\left(\mathbf{r},\Omega\right)=\mu\frac{\partial I}{\partial x}+\eta\frac{\partial I}{\partial y}+\left(\mathrm{i}\,dim-2\right)\xi\frac{\partial I}{\partial z} \tag{8}$$

In equation (8), μ,η and ξ denotes the cosines of direction along the Cartesian co-ordinate x, y and z directions respectively, $\mathrm{i}\,dim$ denotes the dimensionality of the problem domain in which the value will be 2 for 2D planar geometry and 3 for 3D geometry [44]. Once the distribution of the intensity is known, the heat flux can be determined by the following expression [3, 42, 43, 45]

$$q=\int_{2\pi}I\left(\mathbf{r},\Omega\right)\Omega\cdot\mathbf{n}\,\mathrm{d}\Omega \tag{9}$$

The Discrete Ordinate Method (DOM) and its integration with the mesh

This method transforms the radiative heat equation into a set of simultaneous partial differential equations based on a discrete representation of the directional variation of radiative intensity [3, 35]. The computational domain of the problem is identified and divided into meshes as can be seen in Figure 6.

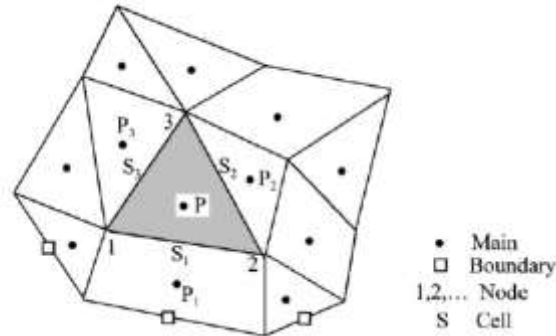# Global Journal of Engineering Science and Research Management

Figure 6. Cell centered control volume in 2D unstructured mesh, taken from [44]

The discretised RTE of equation (6) along the discrete direction $\Omega^m = \left(\mu^m, \eta^m, \xi^m\right)$ over a volume cell and a solid angle once the divergence theorem is applied in the Cartesian coordinate is as follows [44]

$$\sum_{i=1}^{N_P} I_i^m A_i D_i^m = \left[-\left(\kappa + \sigma_s\right) I^m + \kappa I_b + \frac{\sigma_s}{4\pi} \sum_{m'=1}^{M} w^{m'} \phi^{mm'} I^{m'} \right]_P \Delta V_P \qquad (10)$$

In equation (10), N_P, A_i, D_i, I^m and $I^{m'}$ is total surface number for cell P, ith surface area, the product of the normal unit vector at the ith surface and the intensity direction Ω^m, the intensity along direction Ω^m and intensity along direction $\Omega^{m'}$ respectively [44]. $w^{m'}$, ΔV_P and M is the solid angle associated with direction $\Omega^{m'}$, the volume of cell P and the total number of discrete directions respectively [44]. The inflow and outflow of radiant energy passing in the direction Ω^m across all cell surfaces is represented at the left hand side of equation (9) while the attenuation and augmentation of radiant energy passing in the direction Ω^m through the cell volume is represented in the right hand side of equation (10) [44]. The following equation (11) is needed to relate the intensity on the cell surfaces and the cell centre intensity in order to close equation (10) [44]

$$I_i^m = max\left(A_i D_i^m, 0\right) I_P^m - max\left(-A_i D_i^m, 0\right) I_{P_i}^m \qquad (11)$$

In the above equation, P_i is the neighbour cell of cell P with ith surface as the same face between P and P_i while $I_{P_i}^m$ is the intensity at cell P_i. Therefore, the final discretised form of equation (10) becomes [44]

Global Journal of Engineering Science and Research Management

$$\left[\left(\kappa+\sigma_{s}\right)\Delta V_{P}+\sum_{i=1}^{N_{P}}max\left(A_{i}D_{i}^{m},0\right)\right]I_{P}^{m}=\sum_{i=1}^{N_{P}}max\left(-A_{i}D_{i}^{m},0\right)I_{P_{i}}^{m}+$$

$$\left[\kappa I_{b}+\frac{\sigma_{s}}{4\pi}\sum_{m'=1}^{M}w^{m'}\phi^{mm'}I^{m'}\right]_{P}\Delta V_{P} \tag{12}$$

The discretised boundary condition of equation (7) becomes [44]

$$I_{w}^{m}=\varepsilon I_{bw}+\frac{\left(1-\varepsilon\right)}{\pi}\sum_{D_{w}^{m'}>0}^{m'=1,...,M}I_{w}^{m'}D_{w}^{m'}w^{m'},\quad D_{w}^{m}<0 \tag{13}$$

The temperature value at the boundary faces is used to calculate the blackbody intensity as in Equation (3). The value of the blackbody intensity is then substituted in the boundary condition in Equation (7) and (13) since the boundary face is a part of the surface enclosure. The calculation is done element by element until all directions have been covered and the convergence criteria are met.

The Seven Cases Unstructured Triangulation Technique (7CUTT) Algorithm

The contribution of this paper is a new algorithm called the *Seven Cases Unstructured Triangulation Technique* for the initial triangular mesh generation (7CUTT). 7CUTT is a newly developed algorithm for initial unstructured triangulation grid generation with a slight modification to the SAFT in terms of element creation and the control grid. The algorithm of 7CUTT is applicable to the domain with single or multiple inner boundaries. It still uses the concept of the SAFT where the Front is moved into the interior of the domain in a 'marching' process when constructing triangular elements. It must be noted that the terms 'edge', 'Front', 'active edge', 'passive edge', 'active node' and 'ideal point' (IP) in 7CUTT are similar to those explained in SAFT in section 3.1.

The endpoints of outer boundary curves in the domain are the first set of nodes created in order to prepare for the triangular mesh generation. This is followed by all the nodes created at the boundary curves resulting from discretising boundary curves (both inner and outer boundaries) into boundary edges. As illustrated in Figure 7a, the boundary curves are discretised into a number of outer boundary edges (from the outer layer boundary) and a number of internal boundary edges (from the internal boundary layer). It must be noted that in the 7CUTT algorithm, nodes are placed at the location of sensor deployment where a boundary edge is formed automatically between two sensors.

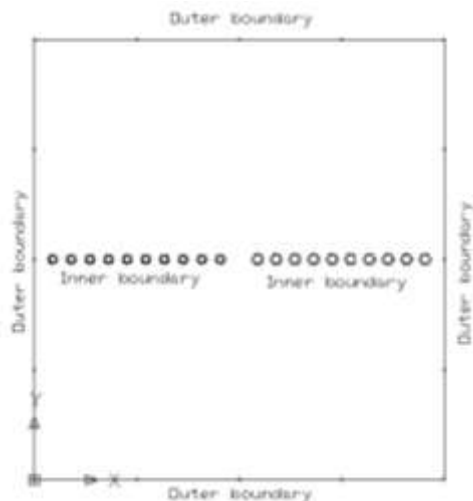# Global Journal of Engineering Science and Research Management

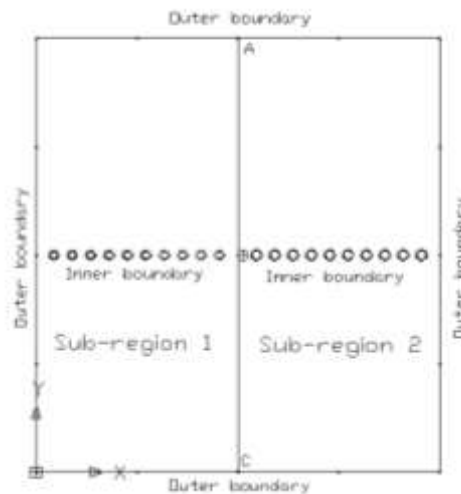Figure 7a. Definition of boundary edges at boundary curves

Figure 7b. The whole domain is divided into sub-regions

The whole domain is then divided into several sub-regions before generating the triangular meshes. Figure 7a illustrates the whole domain with outer and inner boundary layers. As can be seen in Figure 7b, in order to divide the whole domain into sub-regions, newly created line segments (AB and BC) are placed in the middle of the domain by connecting the centre of the domain to the existing nodes at the outer boundary. Once the division of the domain is done, there is another problem that needs to be tackled here in which the newly created line segment in the domain needs to be further discretised into a number of smaller edges. Therefore, a layer concept is proposed to be applied at the boundary of the sub-regions where a line segment can be divided into several line segments or edges with linearly different length. The layer concept can be referred to in Section 4.1.

The layer concept and its significance to the 7CUTT
It must be noted that the layer concept is a novel contribution of this paper. 7CUTT makes use of the layer concept at the appropriate boundary curve or line. The aim of employing the layer concept is to divide a line into several segments with different lengths linearly. The length Ld_i of layer d_i with $i = 1, 2..., m$ is given as

$$Ld_i = i \frac{L}{\sum_{k=1}^{m} k} \qquad (14)$$

In the above equation, L is the total length of the straight line while m is the number of layers needed.

Figure 8a. A straight line AB before applying the layer concept

Figure 8b. A set of nodes are placed at the line segments produced by employing the layer concept at line AB

The line or boundary curve that is divided using the layer concept produces several smaller line segments with different lengths linearly. A set of nodes is placed at the end of each newly divided segment line. Figure 8a illustrates a straight line before having the layer concept while Figure 8b illustrates m number of smaller segment lines or edges resulting from the layer concept applied at AB. For illustration, let us say the length of the straight line AB as in Figure 8a is $L = 1.34$ and the number of layers required is $m = 6$. Table 1 shows the layer and its length for every layer of Figure 8b.

Table 1. The result for layer concept for Figure 8b

Layer d_i	Length of layer, Ld_i	Layer d_i	Length of layer, Ld_i
d_1	$Ld_1 = (1)\dfrac{1.34}{1+2+3+4+5+6} = 0.0638$	d_4	$Ld_4 = (4)\dfrac{1.34}{1+2+3+4+5+6} = 0.2552$
d_2	$Ld_2 = (2)\dfrac{1.34}{1+2+3+4+5+6} = 0.1276$	d_5	$Ld_5 = (5)\dfrac{1.34}{1+2+3+4+5+6} = 0.3190$
d_3	$Ld_3 = (3)\dfrac{1.34}{1+2+3+4+5+6} = 0.1914$	d_6	$Ld_6 = (6)\dfrac{1.34}{1+2+3+4+5+6} = 0.3830$

In the present study, the layer concept is proposed to be applied once the whole domain is divided into sub-regions, where it is employed to generate the segment lines at the appropriate boundary of the sub-region. This can be referred to in Figure 9, where the layer concept is applied at newly created line segments AB and BC. It is shown that the gap length between all the edges is reduced with the existence of these sets of newly created line segments.

Global Journal of Engineering Science and Research Management

Therefore, the layer concept is serving as an interior gradation control as it is incorporated in the algorithm of 7CUTT. However, it must be noted that either the entire Front or specific area needs to be chosen (starting from the edge with the shortest length condition) for the departure zone or the element creation zone in order to have a full effect of gradation control in terms of size using the layer concept.
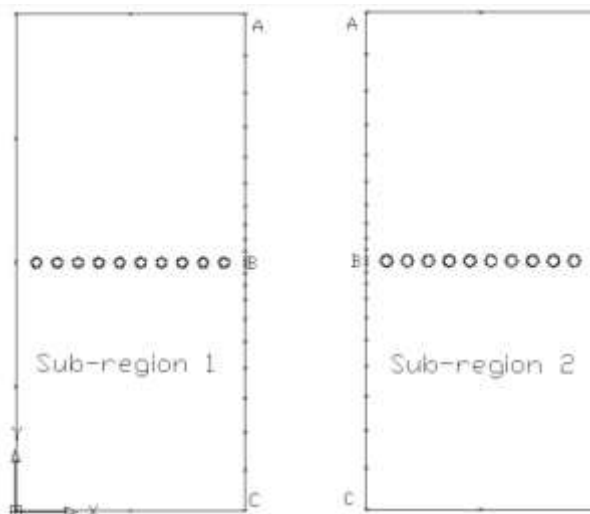

Figure 9. Applying the layer concept at the newly created line segment (the newly created boundary of the sub-regions - AB and BC)

The general idea of the Seven Cases Unstructured Triangulation Technique (7CUTT) and the algorithm

In 7CUTT, the current selected active edge among all the active edges in the Front that is considered for triangular element construction is called the base edge. For example, referring to Figure 10a, of all the active edges in the Front, $(11,12)$ are currently selected for triangular element construction therefore; $(11,12)$ is called a base edge. Once the base edge is identified, the position of IP on the perpendicular bisector of the base edge is computed in such a way that an equilateral triangle is formed with IP as the third vertex. Let us say the length of the base edge is denoted as L_{base_edge}. The easiest way to compute the IP satisfying the above condition is to form a circle (with a radius equal to L_{base_edge} and centred at the nodes respectively) at each node of the base edge as illustrated in Figure 10a. Basically, there are two intersection points at first, but the one that lies inside the Front or inside the acceptance

Global Journal of Engineering Science and Research Management

region is chosen. The chosen intersection point of these two circles is the IP. The two circles constructed previously are deleted in order to avoid confusion while the IP remains in the domain as illustrated in Figure 10b.
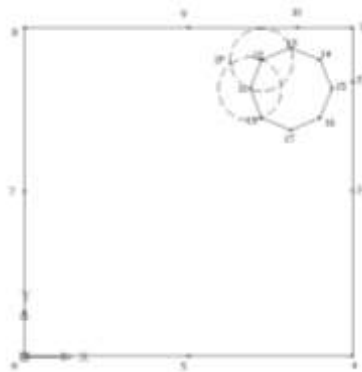

Figure 10a. The base edge is $(11,12)$. Intersection point of the two circles is the IP.
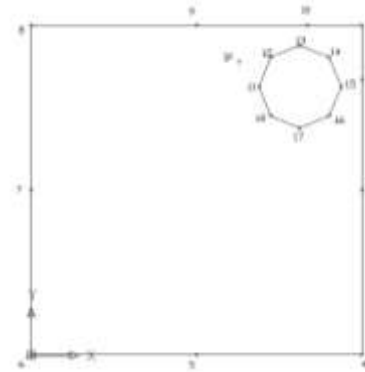

Figure 10b. IP on the perpendicular bisector of the base edge.

A circle with its centre at IP is constructed with a radius, $r = 0.8 * L_{base\_edge}$ as illustrated in Figure 10c. IP becomes the new vertex of the equilateral triangle constructed since there are no active nodes lying within the circle and two newly created active edges are formed automatically as illustrated in Figure 10d. It must be noted that once the triangular element is constructed, the Front needs to be updated in which the base edge becomes a passive edge and is deleted from the Front list. At the same time, the newly created active edges are added to the Front list. Having Figure 10d as an example, $(11,12)$ is deleted and newly created edges which are $(11,19)$ and $(19,12)$ are added to the Front list.
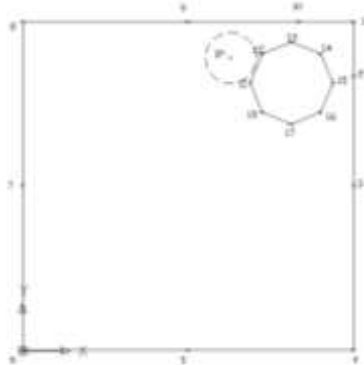
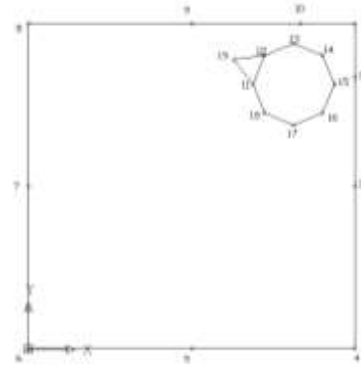Figure 10c. A circle is constructed with IP as centre

Figure 10d. A triangular element is constructed by having IP as the node

The same procedure is repeated to construct the next triangular element, in which base edge is selected, IP is constructed and a circle with radius equal to eighty percent of the length of the base edge and its centre at IP is constructed. A construction of triangular elements using the algorithm of 7CUTT is actually based on the condition of objects lying within the circle or at the circum circle. The term 'objects' in 7CUTT refers to any active nodes or active edges. This is where the construction of the initial unstructured triangular element is based on seven cases of consideration during the element creation procedure according to the 7CUTT algorithm.

The seven cases of consideration for the element creation procedure

Case 1:

The first case (Case 1) is the simplest one in which the current base edge considered is (a,b) as in Figure 11a. A circle at centre IP with $r = 0.8 * L_{base\_edge}$ is constructed. IP becomes the third vertex of the triangular element if there is no object lying within the circle in which it automatically changed to node c as in Figure 11b. The newly created active edges (a,c) and (b,c) become the sides of the triangular element. The element constructed is an equilateral triangle since all three sides or edges have equal length as illustrated in Figure 11b.

Figure 11a. No object lies within the circle   Figure 11b. An equilateral triangle is constructed

Case 2:

The current base edge considered is (a,b) as illustrated in Figure 12a. A circle at centre IP with $r = 0.8 * L_{base\_edge}$ is constructed. There are two objects that lie within the circle. The first one is node d and the second object consists of two active edges intersected with the circle which are (c,d) and (d,e). Priority is given to nodes when it comes to selection if both objects occur simultaneously within the circle. If there are multiple active nodes in the circle, calculate all the distances of every active node to the IP. The active node which is the closest one to the IP is selected as the third vertex for triangular elements. As illustrated in Figure 12b, node d is selected as the vertex; therefore, a triangular element is constructed with (a,b), (a,d) and (b,d) as the three sides.

Figure 12a. Two types of the object lie within the circle   Figure 12b. Triangular element is constructed with
which are active nodes and active edges   edge (b,d)

Case 3:

At the same time, there is another triangular element being constructed automatically since the three edges are

Global Journal of Engineering Science and Research Management

connected to themselves. This condition belongs to Case 3. As illustrated in Figure 12b, a triangular element is constructed automatically when (b,d) is formed. The three edges (b,c), (c,d) and (b,d) are connected to themselves, and they become the sides of the second triangular element.

Case 4:

Figures 13a and 13b show the construction of a triangulation element following Case 4. Let us say the base edge considered is (a,b), where a circle at centre IP with $r = 0.8 * L_{base\_edge}$ is constructed. Based on the figure, it can be seen that the only object involved is an active edge which is intersected with the circle. The active edge intersected with the circle is (b,c) as illustrated in Figure 13a. The intersection point of the circum circle with (b,c) is marked as point $p1$ and $p2$. Based on the algorithm of 7CUTT, the length between the intersection points, L_{p1p2} needs to be determined. In order words, referring to Figure 13a the length between $p1$ and $p2$ needs to be determined. If the length is less than the radius of the circle or $L_{p1p2} < r$, therefore, the intersected active edge is disregarded and IP becomes the third vertex of the triangular element. Based on Figure 13b, the IP becomes node d in which a triangular element is constructed with edges (a,b) (a,d) and (b,d) as the three sides of the triangular element.
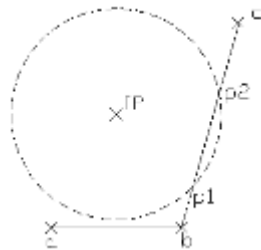

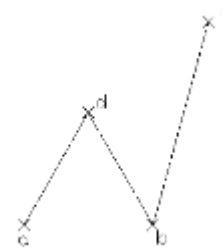Figure 13a. An active edge intersected with the circle   Figure 13b. The IP becomes the new active node for the triangular element

Case 5:

Let say the whole length of the intersected active edge is denoted as L_{ie}. Slightly different from Case 4, if $L_{p1p2} \geq r$ and at the same time, $L_{ie} < 2 * L_{base\_edge}$, therefore, the active edge intersected with the circle is considered in which the node of the intersected active edge is selected as the third vertex. In other words, referring

to Figure 14a, let say the base edge being considered is (a,b). Since the length of $p1$ and $p2$ is more than the length

of r, and the length of (b,c) is less than double the length of (a,b) therefore, node c is selected to be the vertex to

form the triangle element as illustrated in Figure 14b. However, if there are multiple edges intersected with the circle and they all satisfy the conditions of Case 5, therefore, the associated node which is the closest to IP is selected as the third vertex.
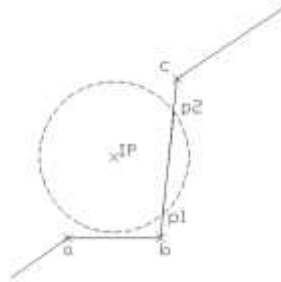

Figure 14a. The intersected active edge is (b,c). The length of intersection point $p1$ and $p2$ with the circle is more than the length of the radius and at the same time $L_{ie} < 2 * L_{base\_edge}$
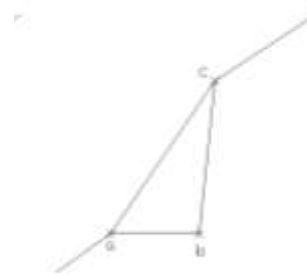
Figure 14b. The triangular element is constructed by connecting the node associated with the intersected active edge with the base edge.

Case 6:

There are three conditions that need to be satisfied for Case 6. The first one is $L_{p1p2} \geq r$. The second condition is

$L_{ie} \geq 2 * L_{base\_edge}$. The third condition is that the IP must be outside the existing element and the ratio between the

length of the perpendicular line of the intersected active edge connecting directly to the IP and the length of the

intersected active edge must be less than 0.1, $\frac{L_p}{L_{ie}} < 0.1$. Once all the three conditions are satisfied simultaneously,

therefore, the active edge intersected with the circle is considered in which the node of the intersected active edge is selected as the third vertex. Let say the base edge being considered for Case 6 is (a,b). In other words, referring to

Figure 15a, since the length of $p1$ and $p2$ is more than the length of the radius, the length of intersected active edge

which is (b,c) is more than double the (a,b), and at the same time $\frac{L_p}{L_{(b,c)}} < 0.1$, therefore, node c which is the node

Global Journal of Engineering Science and Research Management

associated with active edge (b,c) is selected to be the vertex to form the triangle element as illustrated in Figure 15b. However, if there are multiple edges intersected with the circle and they all satisfy the conditions of Case 6, therefore, the associated node which is the closest to IP is selected as the third vertex.
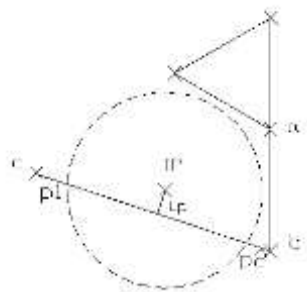

Figure 15a. The intersected active edge is (b,c). The three conditions which are $L_{p1p2} \geq r$, $L_{(b,c)} \geq 2 * L_{(a,b)}$ and $\dfrac{L_p}{L_{(b,c)}} < 0.1$ are satisfied.

Figure 15b. The triangular element is constructed by connecting the node associated with the intersected active edge to the base edge.

Case 7:

There are three conditions that need to be satisfied for Case 7. The first one is $L_{p1p2} \geq r$. The second is $L_{ie} \geq 2 * L_{base\_edge}$. The third condition is that the IP must be outside the existing element and $\dfrac{L_p}{L_{ie}} \geq 0.1$. Once all the three conditions are satisfied simultaneously, then there will be two new elements to be constructed following Case 7. The first one is when the IP becomes a new node and it is connected to the base edge. The second element is when the intersected active edge is connected to the new node. Let us say the base edge being considered for Case 7 is (a,b). Referring to Figure 16a, active edge (b,c) is intersected with the circle in which the length of $p1$ and $p2$ is more than the length of the radius and the length of (b,c) is more than double the length of (a,b). Since the IP is out of the existing element, a perpendicular line of (b,c) connecting directly to the IP is created. The ratio of the
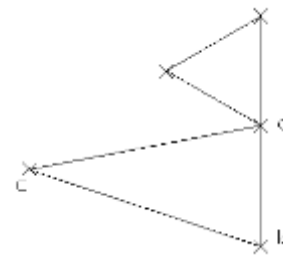
Global Journal of Engineering Science and Research Management

length of perpendicular line to the length of (b,c) is more than 0.1. Therefore, two elements are constructed in which the IP becomes node d and both (a,b) and (b,c) is connected to d as in Figure 16b.
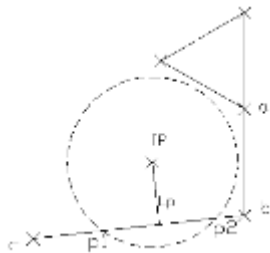

Figure 16a. The intersected active edge is (b, c). The three conditions, $L_{p1p2} \geq r$, $L_{(b,c)} \geq 2*L_{(a,b)}$ and $\dfrac{L_p}{L_{(b,c)}} \geq 0.1$ are satisfied.
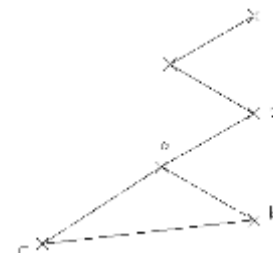
Figure 16b. The triangular element is constructed by connecting the node associated with the intersected active edge to the base edge.

The departure zone in 7CUTT for the element creation procedure
In order to prepare for generation of new nodes and edges inside the domain, the classification of edges for the initial Front in every sub-region requires special definition. The edge is denoted as (a,b) which is composed of node a and b where $a,b \in (x_i, y_i)$. (x_i, y_i) is the coordinate of the node and $i = 1,2,3........$ Reference number of each inner boundary edge is $r_j = (a,b)$ where $j = 1, 2,..p$ and p is the total number of inner boundary edges in the whole domain. The reference number of each outer boundary edge is $r_k = (a,b)$ where $k = p+1, p+2,....p+q$ and q is the total number of outer boundary edges in the whole domain. The reference number of each edge from the layer concept at the sub-region boundary is $r_l = (a,b)$ where $l = p+q+1, p+q+2,...., p+q+n$ and n is the total number of edges from the layer concept. The initial Front for every sub-region is constructed based on the edges contained or forming the sub-region respectively where it is composed by three categories of edges defined above.

   The departure zone of the 7CUTT is the specific parts of the Front which satisfy certain properties (the length of the edge or angle) starting from the shortest edges. It must be noted that 7CUTT gives priority to inner boundary edges when it comes to constructing triangular elements in the initial Front list. Since the departure zone is not the entire Front, therefore, those edges that satisfy the properties of the departure zone are grouped together in every

updated Front.

The triangulation process starts with the first sub-region. The shortest edge among r_j that belongs to the first sub-region is selected as the base edge for the first triangular element construction. Once the first triangular element is constructed, then the base edge becomes the passive edge and it is deleted from the initial Front list. The reference number of newly created active edges onwards is $r_t = (a,b)$ where $t = p+q+n+1, p+q+n+2, .p+q+n+3, ...$ in which the number is increased by one every time a new edge in the whole domain is created. The next shortest active edge among r_j that belongs to the first sub-region is selected as the base edge and the same procedure is repeated until r_j of the first sub-region become passive edges.

Once all r_j of the first sub-region have completely become passive edges, the next shortest active edges from the departure zone group of the initial Front that belong to the first sub-region are selected as base edges for the next triangular element construction. The same procedure is repeated until all the active edges from the departure zone group of initial Front become passive and are deleted from the list.

The second Front list for the first sub-region is then constructed, which is composed of all the remaining newly created active edges r_t together with the available active edges from initial Fronts previously. Again, the departure zone for element construction is the specific parts of the second Front which satisfy certain properties (the length of the edge or angle) starting from the shortest edges. The same procedure is repeated until all the active edges from the departure zone group of second Front become passive and are deleted from the list.

The third Front is constructed by all the remaining newly created active edges r_t together with the available active edges from the second Front previously. The same procedure is repeated until there is no more active edge to form the Front list, or in other words the entire first sub-region is covered. The triangulation process is then continued with the second sub-region until the final sub-region where the same procedure is repeated as the triangulation process explained for the first sub-region above.

In order to illustrate the concept of departure zone in 7CUTT, Figure 17a-Figure 17h are used. Figure 17a illustrates all 17 edges that form the initial Front before the creation of the triangular element mesh. The initial Front is composed of edges $r_3, r_4, r_9, r_{10}, r_{23}, r_{24}, r_{25}, r_{26}, r_{27}, r_{28}, r_{29}, r_{30}, r_{31}, r_{32}, r_{33}, r_{34}, r_{35}$. $r_3 r_4$ are the inner boundary edges while $r_9, r_{10}, r_{23}, r_{24}$ are the outer boundary edges formed by the sensor deployment. The edges $r_{25}, r_{26}, r_{27}, r_{28}, r_{29}$ at the

Global Journal of Engineering Science and Research Management

upper boundary and $r_{30}, r_{31}, r_{32}, r_{33}, r_{34}, r_{35}$ at the right boundary are the edges formed from the layer concept applied on the sub-region boundary curves. It must be noted that the chosen departure zone in this example is the inner boundaries and the edges from the layer concept. Figure 17b shows the construction of the first and second triangular elements among the inner boundary edges. r_{47}, r_{48}, r_{49} and r_{50} are the newly created active edges while r_{3} and r_{4} become passive edges.
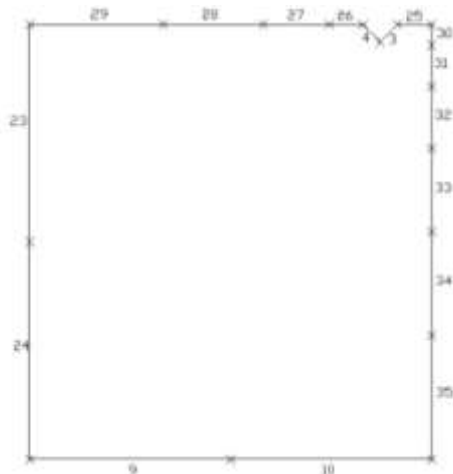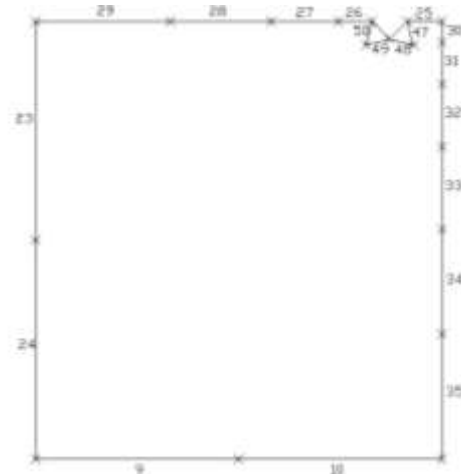

Figure 17a. The initial or first Front

Figure 17b. The first and second triangular element creation in the Front

Figure 17c illustrates the third and the fourth element creations. Figure 17d illustrates the element creation at the remaining active edges belonging to the departure zone group. It must be noted that all active edges of the departure group of the initial Front should become passive then only the new second Front lists will be formed. The second Front is composed by the newly created active edges together with the remaining active edges where in this example it is $r_{48}, r_{49}, r_{53}, r_{54}, r_{55}, r_{56}, r_{57}, r_{58}, r_{59}, r_{60}, r_{61}, r_{62}, r_{63}, r_{64}, r_{29}, r_{35}, r_{23}, r_{24}, r_{9}, r_{10}$ which is numbered as in figure 17d.

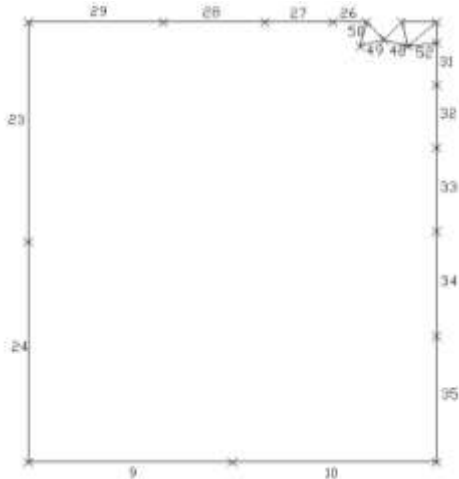# Global Journal of Engineering Science and Research Management

Figure 17c. The third and forth triangular element creation in the Front
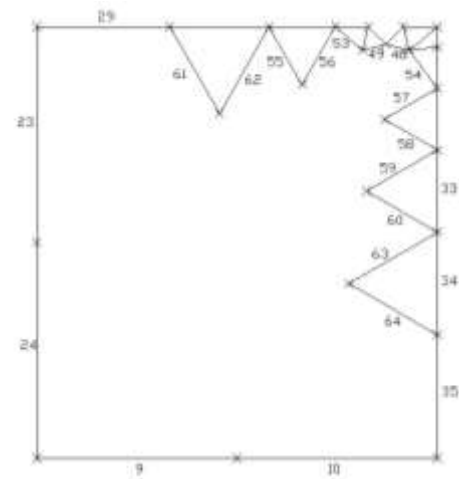

Figure 17d. All the active edges of the departure zone group of the initial Front become passive and form the second Front

The same procedure is repeated with all the edges in the departure zone group until all edges of the departure zone in the second Front become passive. The remaining newly created active edges and the available active edges from the second Front will form the third Front list as in Figure 17e. The third Front as in Figure 17e is $r_{66}, r_{67}, r_{68}, r_{69}, r_{70}, r_{71}, r_{72}, r_{73}, r_{74}, r_{75}, r_{76}, r_{29}, r_{35}, r_{23}, r_{24}, r_{9}, r_{10}$. The same procedure is repeated to form the fourth Front as in Figure 17f. The fourth Front is composed of $r_{77}, r_{79}, r_{80}, r_{81}, r_{83}, r_{84}, r_{85}, r_{86}, r_{87}, r_{88}, r_{89}, r_{90}, r_{91}, r_{23}, r_{24}, r_{9}, r_{10}$.

Global Journal of Engineering Science and Research Management
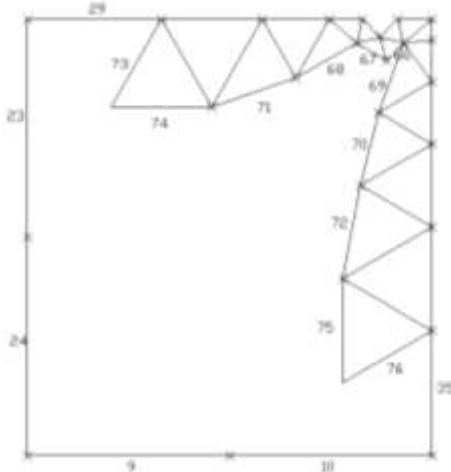

Figure 17e. All the active edges of the departure zone group of second Front become passive and form the third Front
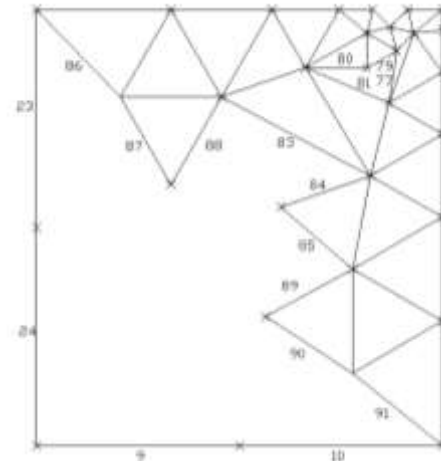

Figure 17f. All the active edges of the departure zone group of the third Front become passive and form the fourth Front

The same procedure is repeated to form the fifth Front as in Figure 17g. The fifth Front is composed of $r_{94}, r_{96}, r_{97}, r_{98}, r_{24}, r_{9}$. The final Front is illustrated in Figure 17h where there are no active edges available for triangulation.

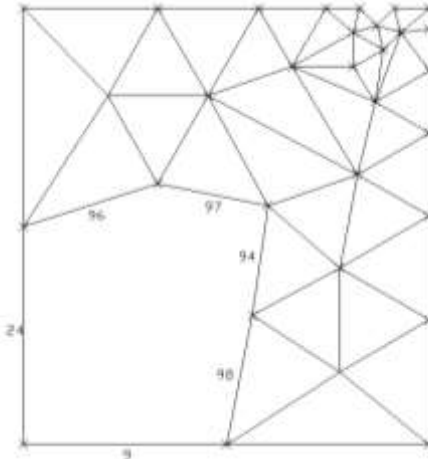Global Journal of Engineering Science and Research Management

Figure 17g. All the active edges of the departure zone group of fourth Front become passive and form the fifth Front.
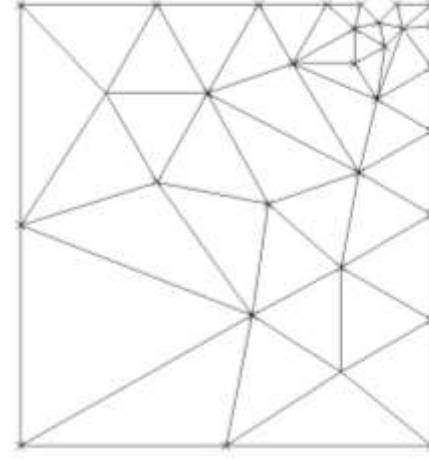

Figure 17h. Triangular element mesh in the sub-region

The 7CUTT with specific Front as departure zone starting with the shortest edge is summarized as follows:

Step 1: Generate nodes at the outer boundary based on the pre-determined location on the sensors. Generate inner boundary nodes. The whole computational domain is then divided into M number of sub-regions. Apply the layer concept at the desired location along the boundary of the sub-region.

Step 2: From the nodes at the boundary, boundary edges will be formed. The set of all boundary edges (at outer, inner boundary as well as at sub-region boundary) will now be the Initial Front. Start to generate triangular elements at sub-region 1.

Step 3: The inner boundary edge will be chosen first to be triangulated. The current selected edge being considered is called the base edge.

Step 4: Compute the ideal point (IP) on the perpendicular bisector of the base edge in such a way that an equilateral triangle is formed with the IP as vertex.

Step 5: Construct a circle with a radius $r = 0.8 * L_{base\_edge}$. Determine if any objects such as active nodes lie within the circle or intersected active edges with the circum circle.

Step 6: Generate the triangular elements based on the seven categories of cases below:

Case 1: No active nodes or active edges lie within the circle. The IP is selected as the vertex. Equilateral triangle will be formed.

Case 2: Active nodes lie within the circle. Compute the distance of all the active nodes and the IP. The closer point to the IP will be selected as the vertex.

Case 3: Three active edges are connected to themselves. Therefore, the three edges will automatically form a triangular element.

Case 4: No active node lies within the circle. However, there is an active edge intersecting with the circle but $L_{p1p2} < r$. Therefore, the intersected active edge is disregarded and instead the IP will become the vertex.

Case 5: No active node lies within the circle. However, there is active edge intersecting with the circle. At the same time, both $L_{p1p2} \geq r$ and $L_{ie} < 2*L_{base\_edge}$ are satisfied. Therefore, the nodes associated with the intersected edge will be considered in which the node that is closer to the IP will be selected as the vertex to form a new element.

Case 6: No active node lies within the circle. However, there is an active edge intersecting with the circle. At the same time, three conditions $L_{p1p2} \geq r$, $L_{ie} \geq 2*L_{base\_edge}$ and $\dfrac{L_p}{L_{ie}} < 0.1$ are satisfied. Therefore, the active edge intersecting with the circle is considered in which the node of the intersected active edge is selected as the third vertex.

Case 7: No active node lies within the circle. However, there is an active edge intersecting with the circle. At the same time, three conditions $L_{p1p2} \geq r$, $L_{ie} \geq 2*L_{base\_edge}$ and $\dfrac{L_p}{L_{ie}} \geq 0.1$ are satisfied. Therefore, two new elements will be constructed.

Step 7: Update the Front by deleting the base edge. The new active edges created during the triangulation element will be added in the Front list.

Step 8: If there are still inner boundary edges left, repeat Steps (4) to (7) until all inner boundary edges have been triangulated from the Initial Front list. If there is only one inner boundary edge, go directly to Step (9).

Step 9: Select the active edge with the shortest length in departure zone group. The current selected edge being considered is called the base edge. Repeat Step (4) - Step (7) until all the active edges in the departure zone group in the current Front become passive.

Global Journal of Engineering Science and Research Management

Step 10: Construct a new Front list composed of all the newly created edges together with the available active edges from the previous Front.

Step 11: Select the active edge with the shortest length in the departure zone group of the latest updated Front list. The current selected edge being considered is called the base edge. Repeat Step (4)-Step (7) until all the edges of the departure zone become passive edges.

Step 12: Step (10) - Step (11) are repeated until there is no more active edge to compose the Front, which means the entire sub-region 1 has been completely triangulated.

Step 13: Repeat Step (3) - Step (12) for the next sub-region until all M number of sub-regions have been triangulated, which means that the whole computational domain has been completely triangulated.

The newly created post-processing procedure

In 7CUTT, there are times where the existing post-processing procedure may not be appropriate to be used in order to improve the quality of the mesh. This is when the existing post-processing procedures such as the diagonal swapping [12, 40, 46] and the Laplace mesh smoothing [21, 25] do not have an impact when there is more than one poor element side by side or in between the elements. Therefore, a new procedure is created to cater for this kind of problem when using 7CUTT and it is called as 7CUTT polygon refinement procedure.

The first step of the 7CUTT polygon refinement procedure is identifying the elements with poor quality as in Figure 18a. The adjacent elements which have good quality will be subdivided at their centroid as in Figure 18b. The poor elements together with the newly developed element which share the same edge with the poor element will be deleted and become a new polygon as in Figure 18c. The new polygon will then be subdivided at their centroid as in Figure 18d. It must be noted that the total number of the elements will be increased using this procedure in order to improve the quality of the mesh.

Global Journal of Engineering Science and Research Management
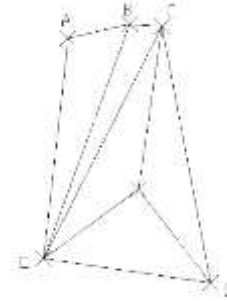

Figure 18a. ABE and BCE are poor elements

Figure 18b. Adjacent element is subdivided at the centroid

Figure 18c. A new polygon is formed when the poor elements and the newly developed element which share the same edge with the poor elements are deleted
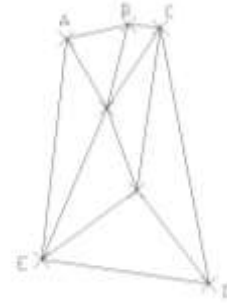

Figure 18d. New elements are created when the polygon is subdivided at the centroid

The significance of 7CUTT

The significance of the 7CUTT can be listed as follows:

1. No grid cell parameters for all elements are required in 7CUTT. The size of the triangular elements that will be generated in the whole domain is controlled by the layer concept applied at desired boundaries as well as the boundary edges from the pre-determined location of the sensors and the inner boundary edges. Therefore, no interpolation of the size parameter is needed at every node every time the element is created.

2. No empirical rule of Equation (1) is needed to calculate the radius of the circle as in SAFT. In order to construct the circle for seven cases of consideration, the radius is set to be eighty percent of the length of the base edge considered. Consequently, the role of calculating the radius in the algorithm of 7CUTT is smaller compared to the SAFT.

3. Seven categories of cases or conditions are identified (select only one case for element creation procedure) in order to determine how to generate the triangular element using 7CUTT. This is an extension of the existing cases of the SAFT. As a matter of fact, the seven categories of cases are able to solve the problem of the need to erase a few existing elements or the need to re-order the Front when there is undecided element creation in the iteration as stated in [12] and [25].

4. A stitching method of connecting the boundary triangular element with the inner triangular element is automatically provided within the same algorithm in 7CUTT. It is guaranteed to connect the boundary element and the ideal triangulation element (equilateral triangle) in the computational domain. Hence, no additional temporary layer of near boundary elements needs to be generated as proposed in [23] for the stitching method.

Integration of the unstructured grid with the governing equation of radiative heat transfer
The sensors placed along the wall in this conceptual model can assist in calculating the initial intensity at the boundary of the enclosure using the equations in Section 3.2. It must be noted that in order to have initial intensity values at the boundary, the function of the sensors is to collect the value of temperatures at the wall. Let us say Nodes N_i ($i = 1, 2, ...n$) are the outer boundary nodes and at the same time, all of these nodes represent the predetermined location of the sensors. The boundary edge is formed by connecting these sensors at the enclosure, and these sensor boundary edges are denoted as $Edge\_sensor_i = (N_i, N_{i+1})$.

As a matter of fact, these sensor boundary edges are among the edges forming a triangular element. Let us say the temperature obtained from the sensors at the outer boundary node N_i are denoted by T_i. The average temperature value of $Edge\_sensor_i = (N_i, N_{i+1})$ at the boundary or at the enclosure will be:

$$TEdge\_sensor_i = \frac{T_i + T_{i+1}}{2} \qquad (15)$$

Once the value of $TEdge\_sensor_i$ is obtained, the value will be replaced in the T of Equation (3) in order to get the value of blackbody intensity. Therefore, Equation (3) can be rewritten as

$$I_b = E_b / \pi = \sigma \left(TEdge\_sensor_i\right)^4 / \pi \qquad (16)$$

The intensity of blackbody obtained from the above equation is substituted in the boundary condition in Equation

(7) and Equation (13), since the boundary face is a part of the enclosure surface. The calculation is done element by element until all directions have been covered and the convergence criteria are met.

The difference between SAFT and 7CUTT

Both SAFT and 7CUTT set up a group of oriented line segments connecting nodes on the boundary as an initial Front. A background grid composed of a minimum number of elements is generated in SAFT and all the nodes of this element are specified with the grid cell parameters (size δ, stretching s and orientation of the cells ϕ). Then, the grid cell parameters for all nodes in the Front are interpolated when constructing the triangular element in the domain in SAFT. On the other hand, no parameters are needed for 7CUTT where a user only needs to specify how many sensors are needed together with their location of employment, the number of reading points or nodes at the inner boundary as well as generating nodes using the layer concept at appropriate boundaries.

In SAFT, the active edge in the Front with the shortest length is selected and it does not matter if it starts with inner boundary edges or outer boundary edges. However, priority is given to inner boundary edges in 7CUTT, where the shortest length of edges is selected. It must be noted that the 7CUTT requires all the inner boundary edges to become passive in the initial Front, which means that the entire set of inner boundary edges have been completely triangulated, and only then will be continued with the rest of the active edges in the Front.

SAFT requires the empirical rule as in Equation. (1) to obtain the radius of the circle for element creation procedure while 7CUTT uses a simpler method where the radius is set to be eighty percent of the base edge. Besides that, in order to determine the construction of equilateral triangles in SAFT, the only condition that needs to be satisfied is that there are no such active nodes lying within the circle. However, the condition for 7CUTT is stricter in which no objects such as active nodes as well as intersected active edges are allowed to lie within the circles when constructing equilateral triangles except for case 7. In general, the 7CUTT has come out with a set of structured 7 categories of cases when constructing the triangular element and not in SAFT.

SIMULATION RESULTS AND DISCUSSION

Simulation is performed using FLUENT on an arbitrary number of sensors placed at various points along the inner wall of the furnace as can be seen in Figure 1b. A set of nodes is placed at the pre-determined location of the sensor where a set of 16 boundary edges are generated. The layer concept is applied at four outer boundary edges near the reactor coil at the left and right side of the furnace. Each of these selected outer boundary edges is divided into three edges of linearly varying length. Therefore, the total number of outer boundary edges is now 24. A total number of 20 inner boundary edges representing the inlet and outlet reactor coils are discretised into eight inner boundary edges for each circle or coil. The whole domain is divided into two sub-regions as illustrated in Figure 9. The layer concept is also applied at the boundary of the sub-regions with 11 edges of varying length linearly, which is at line

segment AB and BC respectively as in Figure 9. The chosen departure zone for this model is all inner boundary edges as well as the edges from the layer concept at line segment AB and BC with the added condition that the length of edges must be less than 0.3763.
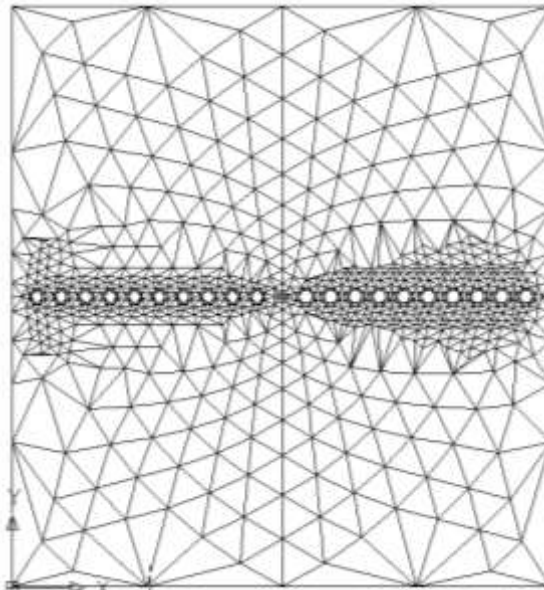

Figure 19. The resulting initial mesh using the algorithm of 7CUTT for a furnace

Figure 19 illustrates the result of an initial unstructured triangular mesh using 7CUTT for a two dimensional representation of an ethylene furnace. The total number of elements generated in the initial mesh is 1680. A magnified view of the initial unstructured mesh at the inlet and outlet reactor coils of Figure 19 is shown in Figure 20a and Figure 20b respectively. All triangular elements covering the computational domain are definitely not of equal size. The boundary elements at the furnace wall (except those boundary elements near the extreme left inlet reactor coil and near the extreme right outlet reactor coil) are greater compared to the rest of the elements since in this specific problem, it is required that the location of the pre-determined sensors themselves are regarded as the nodes forming the boundary elements. The triangular elements near the inlet and outlet reactor coils as in Figure 20a and Figure 20b are very small because those elements are constructed and spanned over the edge with very short

Global Journal of Engineering Science and Research Management

length. It must be noted that the set of inner boundary edges which represent the inlet and outlet reactor coils are among the shortest edges in the domain.
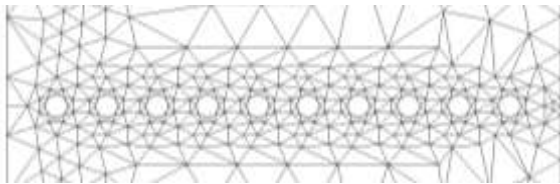

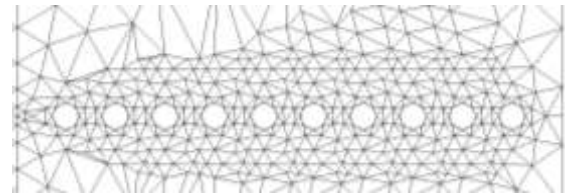Figure 20a. Zoom of the initial unstructured triangular elements at the inlet reactor .

Figure 20b. Zoom of the initial unstructured triangular elements at the outer reactor coils

The sizes of the triangular elements gradually increase from the centre of the furnace where the reactor coils are located towards the furnace wall. This is because the set of edges of varying length linearly which results from the layer concept applied at the boundary of the sub-domain, can tolerate the difference between the shortest length of edges (at the inner boundary) and the longest length of edges (at the outer boundary). Therefore, the element size is increasing gradually with the existence of edges from the layer concept, since the creation of the triangular element in 7CUTT is based on the inner boundary edges and edges from the layer concept at the boundary of sub-regions as the departure zone starting with the shortest active edges.

In order to examine the quality of the mesh, an EquiAngle Skew Q_{EAS}, which is a normalized measure of skewness that is defined as follows is used [47]

$$Q_{EAS} = max\left\{ \frac{\theta_{max} - \theta_{eq}}{180 - \theta_{eq}}, \frac{\theta_{eq} - \theta_{min}}{\theta_{eq}} \right\} \qquad (17)$$

In the above equation, θ_{max} and θ_{min} are the maximum and minimum angles (in degrees) between the edges of the triangular element and θ_{eq} is the characteristic angle corresponding to an equilateral element of a triangular element where in this particular case, $\theta_{eq} = 60°$. The value of the examined quality based on this equation provided by [47] is in the range of $0 \le Q_{EAS} \le 1$ where $Q_{EAS} = 0$ if the element is an equilateral triangle and $Q_{EAS} = 1$ if the triangular element is degenerate (poorly shaped). Figures 21a – Figure 21f illustrate the corresponding triangular elements in the mesh with respect to the range of the quality examined.
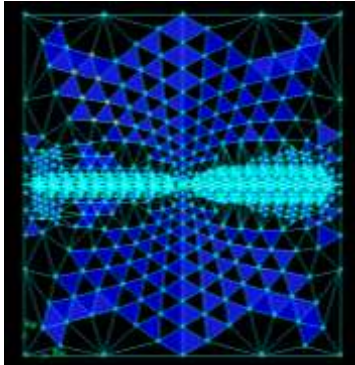
Global Journal of Engineering Science and Research Management

Figure 21a. Element with quality $Q_{EAS} = 0$

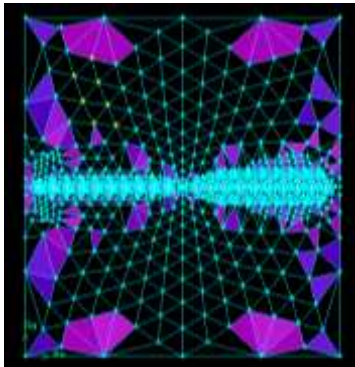

Figure 21b. Element with quality $0 < Q_{EAS} \leq 0.25$
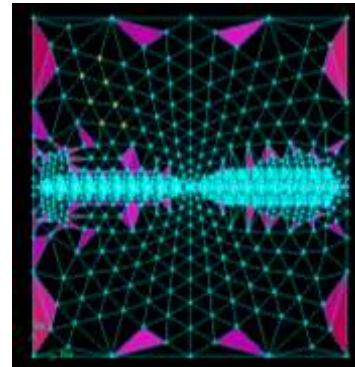

Figure 21c. Element with quality $0.25 < Q_{EAS} \leq 0.5$

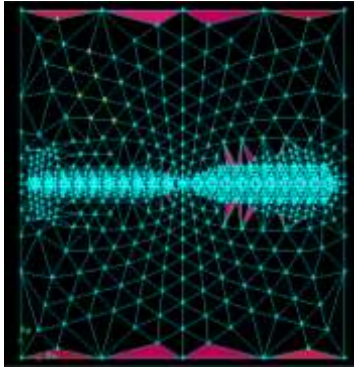Figure 21d. Element with quality $0.5 < Q_{EAS} \leq 0.75$

Figure 21e. Element with quality $0.75 < Q_{EAS} \leq 0.9$

Figure 21f. Element with quality $0.9 < Q_{EAS} \leq 1$

The overall relationship between Q_{EAS} and mesh quality associated with the percentage of the element quality correspondingly is illustrated in Table 2 [47]. Of all the triangular elements generated, 42.4% are equilateral triangles and only 0.24% fall into the sliver range $0.5 < Q_{EAS} \leq 0.75$ where the highest value for the element quality is $Q_{EAS} = 0.91$. Therefore, the initial triangular elements generated using the 7CUTT are all valid and independent of its size. However, mesh post-processing is needed to improve the quality of the initial mesh specifically to those elements with a quality range of $0.75 < Q_{EAS} < 1$.

Table 2. The number of elements in percentages with respect to the range of the quality of the initial unstructured mesh generated with 7CUTT for the furnace.

Q_{EAS}	Mesh quality	The number of elements in percentages
$Q_{EAS} = 0$	Equilateral (Perfect)	42.386%
$0 < Q_{EAS} \leq 0.25$	Excellent	16.13%
$0.25 < Q_{EAS} \leq 0.5$	Good	33.27%
$0.5 < Q_{EAS} \leq 0.75$	Fair	6.55%
$0.75 < Q_{EAS} \leq 0.9$	Poor	1.43%
$0.9 < Q_{EAS} \leq 1$	Very poor (Sliver)	0.24%
$Q_{EAS} = 1$	Degenerate	0

Global Journal of Engineering Science and Research Management

In order to compare the SAFT with the proposed 7CUTT, the SAFT is applied at the same ethylene furnace domain as in Figure 1b. The algorithm of SAFT is implemented in GAMBIT software where the resulted initial unstructured mesh can be referred in Figure 22. The overall relationship between Q_{EAS} and mesh quality [47] associated with the percentage of the element quality correspondingly is illustrated in Table 3. It can be seen that the SAFT failed to construct equilateral (perfect triangle) for the conceptual model. Furthermore, the value of worst quality element created is $Q_{EAS} = 0.924$ with SAFT which is higher than the worst quality with 7CUTT.
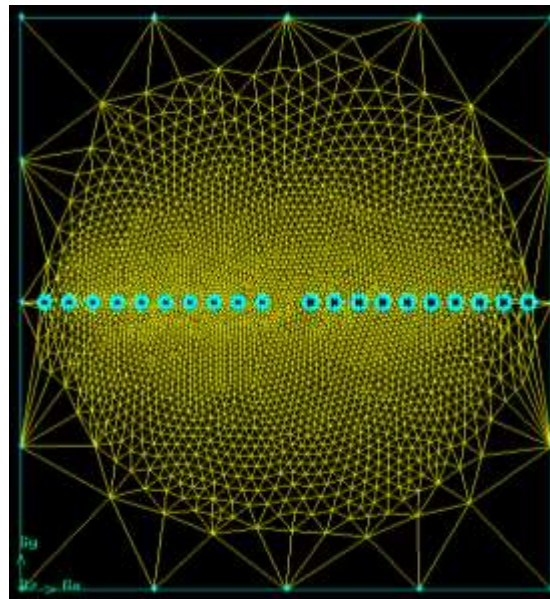

Figure 22. The resulting initial unstructured mesh with SAFT algorithm for the same conceptual model of furnace.

Table 3. The number of elements in percentages with respect to the range of the quality of the initial unstructured mesh generated with SAFT in GAMBIT for the conceptual model of ethylene furnace.

Q_{EAS}	Mesh quality	The number of elements in percentages
$Q_{EAS} = 0$	Equilateral (Perfect)	0

Global Journal of Engineering Science and Research Management

$0 < Q_{EAS} \leq 0.25$	Excellent	90.56%
$0.25 < Q_{EAS} \leq 0.5$	Good	7.3%
$0.5 < Q_{EAS} \leq 0.75$	Fair	1.69%
$0.75 < Q_{EAS} \leq 0.9$	Poor	0.4%
$0.9 < Q_{EAS} \leq 1$	Very poor (Sliver)	0.05%
$Q_{EAS} = 1$	Degenerate	0

Figure 23 illustrates the final unstructured mesh after the mesh post-processing procedure of diagonal swapping, Laplace mesh smoothing and the 7CUTT polygon refinement procedure are applied. The total number of elements after the post-processing becomes 1704 triangular elements. Figures 24a – Figure 24d illustrate the corresponding triangular elements in the final mesh with respect to the range of quality examined after the post-processing procedure. The overall relationship between Q_{EAS} and the mesh quality associate with the percentage of the element quality correspondingly after the mesh post-processing procedure is illustrated in Table 4. It can be seen that the overall quality of the mesh is finally in the range of $0 \leq Q_{EAS} \leq 0.75$.
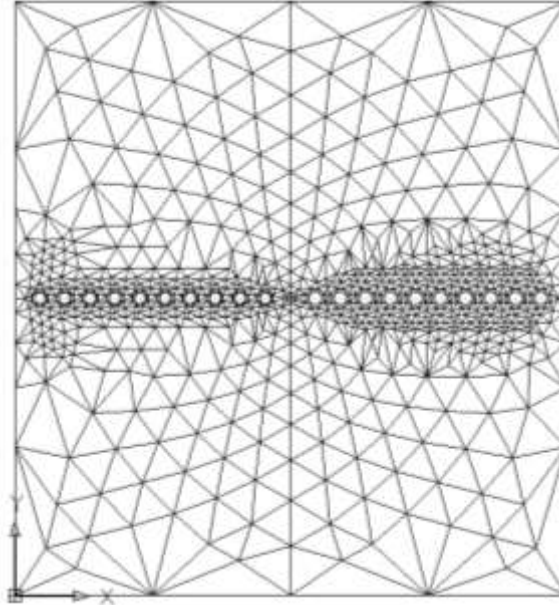
Global Journal of Engineering Science and Research Management

Figure 23. The resulting final mesh after the post-processing procedure

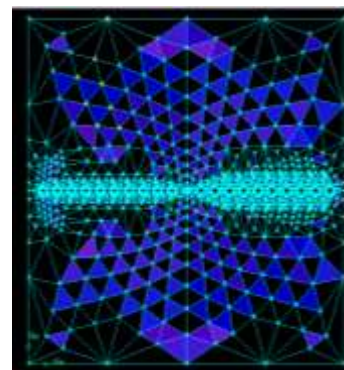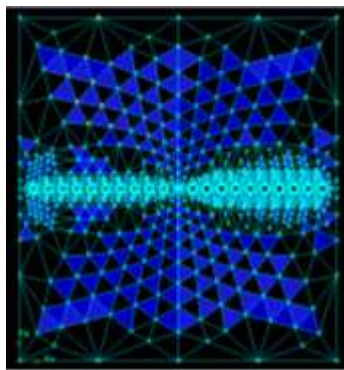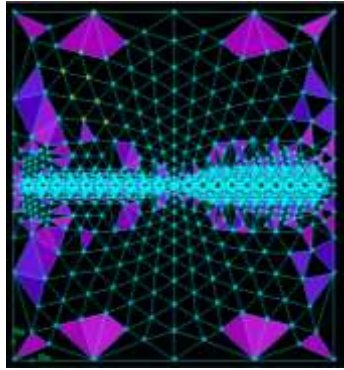Global Journal of Engineering Science and Research Management

Figure 24a. Element with quality $Q_{EAS} = 0$

Figure 24b. Element with quality $0 < Q_{EAS} \leq 0.25$
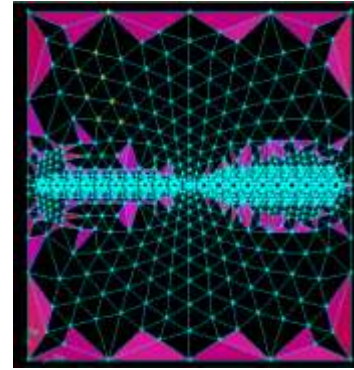
Figure 24c. Element with quality $0.25 < Q_{EAS} \leq 0.5$

Figure 24d. Element with quality $0.5 < Q_{EAS} \leq 0.75$

Table 4. The number of elements in percentages with respect to the range of the quality of the final unstructured mesh generated with 7CUTT for the furnace.

Q_{EAS}	Mesh quality	The number of elements in percentages
$Q_{EAS} = 0$	Equilateral (Perfect)	40.96%
$0 < Q_{EAS} \leq 0.25$	Excellent	16.37%
$0.25 < Q_{EAS} \leq 0.5$	Good	33.74%
$0.5 < Q_{EAS} \leq 0.75$	Fair	8.92%
$0.75 < Q_{EAS} \leq 0.9$	Poor	0
$0.9 < Q_{EAS} \leq 1$	Very poor (Sliver)	0
$Q_{EAS} = 1$	Degenerate	0

In order to prove that the resulted unstructured triangular mesh using the algorithm of 7CUTT works well and is appropriate for computational analysis, the governing equation of radiative heat transfer is incorporated with the mesh of the furnace. Using FLUENT version 6.0, simulation was conducted to solve the radiative heat transfer by using the Discrete Ordinate Methods. Since this is a conceptual model, the value of the wall temperature at every

Global Journal of Engineering Science and Research Management

sensor is imposed so that the temperature values can be used as boundary values in the calculation. The simulation is conducted until convergence is reached at iteration 1148 as in Figure 25.
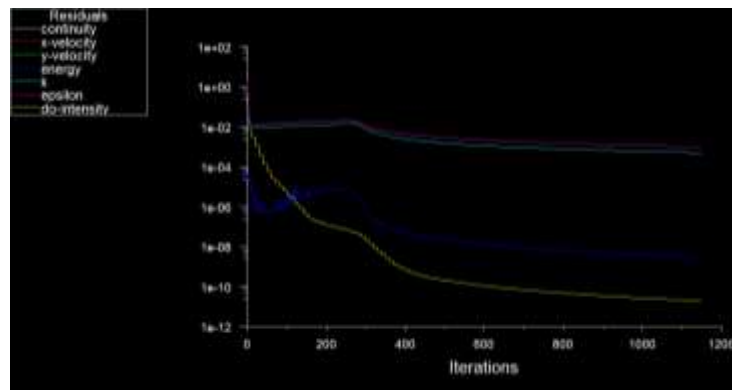

Figure 25. The plot for convergence

The simulation result of the contour plot of temperature (K) distribution for the flue gases in the furnace can be seen in Figure 26. It can be observed that the flue gas temperature decreased when leaving the area of the burner and approaching towards the centre of the furnace with respect to y-direction. As can be seen from the simulation result, the distribution of flue gas temperature in the furnace is not uniform. This scenario influences the heat transfer between the furnace and reactor coils [35]. The result of radiative heat flux (Wm^{-2}) towards the circumference of the reactor coils can be referred to in Figure 27a. The result of the circumferential reactor coils skin temperature can be referred to in Figure 27b. The highest temperature value at the reactor coil skin is 1440.28K, while the lowest temperature value is 1396.12K where the difference is about 44.16K. It can be seen that higher radiative heat flux incident on the reactor coil implies higher reactor coil skin temperature. It is obvious that a pronounced variation of reactor coil skin temperature is obtained since both the heat flux towards the reactor coils and the flue gas temperature in the furnace is not uniform. Referring to [35], the non-uniformity of the heat flux around the reactor coils is caused by the shielding effect of the reactor coils on each other in which resulted in variation of heat flux and reactor coil skin temperature around the circumference of the reactor coils.
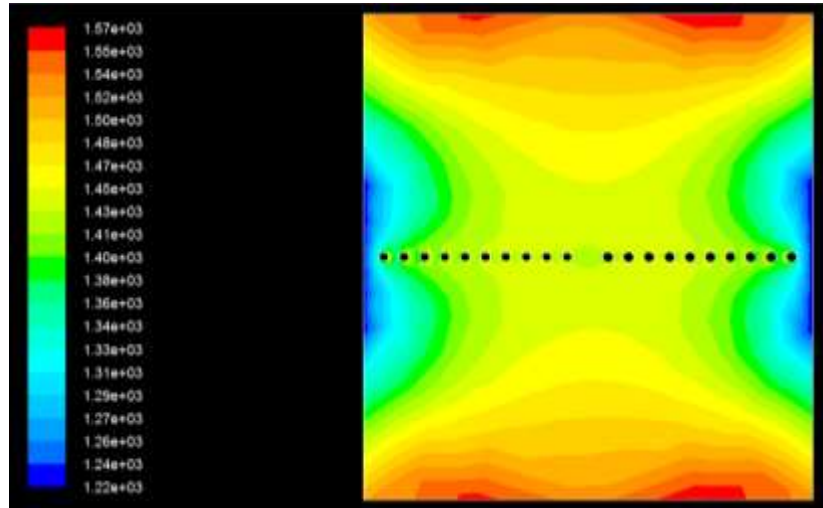
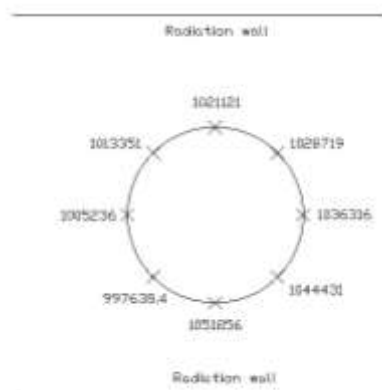Figure 26. The contour of the flue gas temperature in the furnace

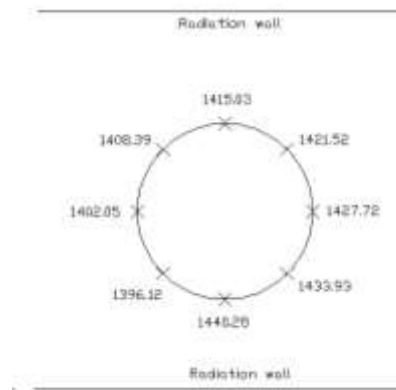Figure 27a. Circumferential heat flux distribution (Wm^{-2})   Figure 27b. Circumferential reactor coil skin
                                                                  temperature (K).

Global Journal of Engineering Science and Research Management

CONCLUSION

A new technique called 7CUTT is proposed which is proven to be effective in generating initial unstructured grids/meshes for modelling the conceptual model of integrating sensors and radiative heat transfer in ethylene cracker furnaces. 7CUTT incorporates the layer concept to generate nodes which form edges of varying lengths linearly at appropriate boundary curves as well as introducing the structured seven cases for the element creation procedure. The differences between 7CUTT and the SAFT are outlined in the paper. The triangular mesh forms the domain for approximating the radiative heat transfer using the Discrete Ordinate Method. Simulations using FLUENT are performed on the triangular mesh to obtain the numerical approximations. The results obtained support the findings in 7CUTT for effectively generating the unstructured mesh in the process of approximating the temperature of flue gas, radiative heat flux incident on the reactor coils as well as the circumferential temperature values of the reactor coils. It must be noted that the novel contribution of the paper is in the method of producing initial unstructured grids, the interior gradation control and the post-processing procedure of improving the quality of resulting meshes, but not the numerical method of the Discrete Ordinate Methods. This fragment should obviously state the foremost conclusions of the exploration and give a coherent explanation of their significance and consequence.

ACKNOWLEDGEMENTS

REFERENCES

Use the "Insert Citation" button to add citations to this document.
Use the "Insert Citation" button to add citations to this document.

1. Gielen, D., K. Bennaceur, and C. Tam. *IEA Petrochemical Scenarios for 2030-2050: Energy Technology Perspectives*. 2006 [cited 2008 17 Dec]; Available from: http://www.iea.org/textbase/work/2006/petrochemicals/Discussion_Paper.pdf.
2. Heynderickx, G.J. and M. Nozawa, *High-emissivity coatings on reactor tubes and furnace walls in steam cracking furnaces.* Chemical engineering science, 2004: p. 5567-5662.
3. Modest, M.F., *Radiative Heat Transfer*. 2 ed. 2003: Academic Press. 822.
4. Abas, Z.A. and S. Salleh, *Extended Advancing Front Technique for the initial triangular mesh construction on a single coil for radiative heat transfer.* The Arabian Journal for Science and Engineering, 2013.

5.   Alias, S., Z.A. Abas, A.S. Shibghatullah, and A.F.N.A. Rahman, *A Brief Review Of Surface Meshing In Medical Images For Biomedical Computing And Visualization* in *International Symposium on Research in Innovation and Sustainability 2014*. 2014, Sci.Int.(Lahore): Malacca, Malaysia.

6.   Abas, Z.A., S. Salleh, S. Ilias, A.F.N.A. Rahman, A.S. Shibghatullah, B.M. Aboobaider, and S. Sidek, *An Insight into the Science of Unstructured Meshes in Computer Numerical Simulation.* Applied Mathematical Sciences, 2014. **8**: p. 8493 - 8516.

7.   Salleh, S. and Z.A. Abas, *Simulation for Applied Graph Theory Using Visual C++*. 2016, Boca Raton, Florida: CRC Press.

8.   Basari, A.S.H., Z.A. Abas, and S. Salleh, *Seven Cases Unstructured Triangulation Technique for Simplified Version of Conceptual Model of Ethylene Furnace for Radiative Heat Transfer Approximation.* International Journal of Computer Applications, 2012. **44**(No 21 April 2012): p. 36-43.

9.   Abas, Z.A. and S. Salleh, *Enhanced Advancing Front Technique with extension cases for initial triangular mesh generation* in *World Congress on Engineering 2011*. 2011: London.

10.   Abas, Z.A., S. Salleh, A.F.N.A. Rahman, H. Basiron, A.S.H. Basari, and N. Hassim, *Improvement of Element Creation Procedure for Generating Initial Triangular Unstructured Mesh for Radiative Heat Transfer Modelling.* International Review on Modelling and Simulation, 2013. **6**.

11.   Lohner, R., *Progress in Grid Generation via the Advancing Front Technique.* Engineering with Computers, 1996: p. 186-210.

12.   Farrashkhalvat, M. and J.P. Miles, *Basic structured grid generation with an introduction to unstructured grid generation*. 2003: Butterworth Heinemann.

13.   Azmi, M.S., N.A. Arbain, A.K. Muda, Z.A. Abas, and Z. Muslim, *Data Normalization for Triangle Features by Adapting Triangle Nature for Better Classification*, in *2015 IEEE Jordan Conference on Applied Electrical Engineering and Computing Technologies (AEECT)*. 2015, IEEE: Jordan.

14.   Abdullah, S.F., A.F.N.A. Rahman, and Z.A. Abas, *Classification of Gender by Using Fingerprint Ridge Density in Northern Part of Malaysia.* ARPN Journal of Engineering and Applied Sciences, 2015. **10**(22).

15.   Abdullah, S.F., A.F.N.A. Rahman, Z.A. Abas, and W.H.M. Saad, *Multilayer Perceptron Neural Network in Classifying Gender using Fingerprint Global Level Features.* Indian Journal of Science and Technology, 2016. **9**(9).

16.   Abas, Z.A., M.R. Ramli, A.S. Shibghatullah, H. Rahmalan, A.F.N.A. Rahman, Z.Z. Abidin, and B. Hussin, *The Implementation of Personal Monitoring System Using Histogram of Gradient, HAAR*

Global Journal of Engineering Science and Research Management

Classifier and Eigenfaces for Human Detection and Recognition. ARPN Journal of Engineering and Applied Sciences, 2015. **10**(19).

17. Hashim, N.A., Z.Z. Abidin, and A.S. Shibghatullah, *Iris Feature Detection using Split Block and PSO for Iris Identification System.* Journal of Telecommunication, Electronic and Computer Engineering (JTEC), 2017. **9**(1).

18. Abdullah, S.F., A.F.N.A. Rahman, Z.A. Abas, and W.H.M. Saad. *Support Vector Machine, Multilayer Perceptron Neural Network, Bayes Net and K-Nearest Neighbour in Classifying Gender Using Fingerprint Global Level Features*. in *2nd International Congress On Technology - Engineering & Science* 2016. Malaysia.

19. Abdullah, S., A. Rahman, Z. Abas, and W. Saad, *Development of a Fingerprint Gender Classification Algorithm Using Fingerprint Global Features.* International Journal of Advanced Computer Science and Applications (IJACSA), 2016. **7**(6).

20. Abas, Z.A., S. Salleh, A.S.H. Basari, and N.K. Ibrahim, *A Conceptual Model Of Integrating Sensor Network and Radiative Heat Transfer Equation for Ethylene Furnace.* AIP Conference Proceedings, 2010. **1309**(1): p. 453-466.

21. Naji, H.S., *An improved advancing front algorithm for triangulating arbitrary two dimensional regions.* 2004.

22. Minyi, K., C. Jie, and J. Huazhong, *Research of Using Dynamic Programming in the Nodes Encoding Optimization*, in *International Conference on Information Engineering and Computer Science, 2009*. 2009.

23. Sazonov, I., D. Wang, O. Hassan, K. Morgan, and N. Weatherill, *A stitching method for the generation of unstructured meshes for use with co-volume solution techniques.* Computational Methods in Applied Mechanics and Engineering., 2006. **195**: p. 1826–1845.

24. Ito, Y., A.M. Shih, A.K. Erukala, B.K. Soni, A. Chernikov, N.P. Chrisochoides, and K. Nakahashi, *Parallel unstructured mesh generation by an advancing front method.* Mathematics and Computers in Simulation, 2007. **75**: p. 200-209.

25. Kovac, N., S. Gotovac, and D. Poljak, *A New Front Updating Solution Applied to Some Engineering Problems.* Archives of Computational Methods in Engineering, 2002. **9**: p. 43-75.

26. Mansor, N., Z.A. Abas, A.F.N.A. Rahman, A.S. Shibghatullah, and S. Sidek, *An analysis of the parameter modifications in varieties of harmony search algorithm.* International Review on Computers and Software (IRECOS), 2014. **9**(10).

Global Journal of Engineering Science and Research Management

27. Mansor, N.F., Z.A. Abas, A. Rahman, A.S. Shibghatullah, and S. Sidek. *An Optimization Solution Using A Harmony Search Algorithm*. in *International Symposium on Research in Innovation and Sustainability (ISORIS 2014)*. 2014. Malacca, Malaysia.

28. Abas, Z.A., Z. Shaffiei, A. Rahman, and A.S. Shibghatullah. *Using Harmony Search for Optimising University Shuttle Bus Driver Scheduling for Better Operational Management*. in *International Conference on Innovative Trends in Multidisciplinary Academic Research (ITMAR-2014)*. 2014. Istanbul, Turkey.

29. Jasmi, M., A. Rahman, Z.A. Abas, and A. Shibghatullah, *Optimized Coating Design of Energy Saving Glass Using Binary Harmony Search for Better Transmission Signal.* International Journal of Computer Science and Information Security, 2016. **14**(8).

30. Shaffiei, Z.A., Z.A. Abas, A.S. Shibghatullah, and A.F.N.A. Rahman, *An Optimized Intelligent Automation for University Shuttle Bus Driver Scheduling Using Mutual Swapping and Harmony Search.* International Journal of Computer Science and Information Security, 2016. **14**(8).

31. Ramli, M.R., Z.A. Abas, N.K. Ibrahim, and B. Hussin, *Solving Complex Nurse Scheduling Problems Using Particle Swarm Optimization.* International Review on Computers and Software (IRECOS), 2016. **11**.

32. Abas, Z.A., L. Ee-Theng, A.F.N.A. Rahman, Z.Z. Abidin, and A.S. Shibghatullah, *Enhanced Scheduling Traffic Light Model Using Discrete Event Simulation for Improved Signal Timing Analysis.* ARPN Journal of Engineering and Applied Sciences, 2016. **10**(18).

33. Ramli, M., Z.A. Abas, F. Arif, and M. Desa, *An Analysis Review Approaches Used In Health Human Resources Planning.* International Journal of Computer Science and Information Security, 2016. **14**(8).

34. Mansor, N.F., Z.A. Abas, A.F.N.A. Rahman, A.S. Shibghatullah, and S. Sidek, *A new HMCR parameter of harmony search for better exploration* Advances in Intelligent Systems and Computing 2016.

35. Lan, X., J. Gao, C. Xu, and H. Zhang, *Numerical Simulation of Transfer and Reaction Processes in Ethylene Furnaces.* Chemical Engineering Research and Design, 2007. **85**(A12): p. 1565-1579.

36. Persson, P.-O., *Lecture 1 Computational Mesh Generation*. 2008, MIT.

37. Zhu, J., T. Blacker, and R. Smith, *Background overlay grid size functions*, in *Proceedings of the 11th international meshing roundtable*. 2002. p. 65–74.

38. Lyra, P.R.M. and D.K. Carvalho, *A computational methodology for automatic two-dimensional anisotropic mesh generation and adaptation.* Journal of the Brazilian Society of Mechanical Sciences and Engineering, 2006. **28**(4): p. 399-412.
39. Seveno, E. *Towards an adaptive advancing front method*. in *6th International Meshing Roundtable*. 1997.
40. Peraire, J., J. Peiro, and K. Morgan, *Advancing front grid generation*, in *Handbook of Grid Generation*, N.P. Weatherill, B.K. Soni, and J.F. Thompson, Editors. 1999, CRC Press LLC.
41. Blazek, J., *Principles of Grid Generation*, in *Computational Fluid Dynamics: Principle and Applications*. 2007.
42. Versteeg, H.K. and W. Malalasekera, *An Introduction to Computational Fluid Dynamics*. 2007, England: Pearson Education.
43. Stefanidis, G., B. Merci, G. Heynderickx, and G. Marin, *Gray/nongray gas radiation modeling in steam cracker CFD calculations.* AIChE Journal, 2007. **53**(7): p. 1658–1669.
44. Liu, J., H.M. Shang, and Y.S. Chen, *Development of an unstructured radiation model applicable for two-dimensional planar, axisymmetric, and three-dimensional geometries.* Journal of Quantitative Spectroscopy & Radiative Transfer 2000. **66**: p. 17-33.
45. Li, B.Q., *Radiative Transfer in Participating Media*, in *Discontinuous Finite Elements in Fluid Dynamics and Heat Transfer*, K.-J. Bathe, Editor. 2006, 3: Germany.
46. Vasiliauskiene, L. and R. Bausys, *Intelligent Initial Finite Element Mesh Generation for Solutions of 2D Problems.* INFORMATICA, 2002. **13**: p. 239–250.
47. *Gambit 2.3 Documentation - Gambit User Guide*.   [cited 2010 25 November]; Available from: http://my.fit.edu/itresources/manuals/gambit2.3/help/index.htm.